



# Diamond channel-cut crystals for high-heat-load beam-multiplexing narrow-band X-ray monochromators

Yuri Shvyd'ko,<sup>a\*</sup> Sergey Terentyev,<sup>b</sup> Vladimir Blank<sup>b</sup> and Tomasz Kolodziej<sup>a,c</sup>

Received 16 May 2021

Accepted 3 August 2021

Edited by M. Yabashi, RIKEN SPring-8 Center, Japan

**Keywords:** X-rays; X-ray optics; Bragg diffraction; diamond; X-ray free-electron lasers.<sup>a</sup>Advanced Photon Source, Argonne National Laboratory, Argonne, IL 60439, USA,<sup>b</sup>Technological Institute for Superhard and Novel Carbon Materials, 142190 Troitsk, Russian Federation, and<sup>c</sup>National Synchrotron Radiation Centre SOLARIS, 30-392 Krakow, Poland.

\*Correspondence e-mail: shvydko@anl.gov

Next-generation high-brilliance X-ray photon sources call for new X-ray optics. Here we demonstrate the possibility of using monolithic diamond channel-cut crystals as high-heat-load beam-multiplexing narrow-band mechanically stable X-ray monochromators with high-power X-ray beams at cutting-edge high-repetition-rate X-ray free-electron laser (XFEL) facilities. The diamond channel-cut crystals fabricated and characterized in these studies are designed as two-bounce Bragg reflection monochromators directing 14.4 or 12.4 keV X-rays within a 15 meV bandwidth to <sup>57</sup>Fe or <sup>45</sup>Sc nuclear resonant scattering experiments, respectively. The crystal design allows out-of-band X-rays transmitted with minimal losses to alternative simultaneous experiments. Only  $\lesssim 2\%$  of the incident  $\sim 100$  W X-ray beam is absorbed in the 50  $\mu\text{m}$ -thick first diamond crystal reflector, ensuring that the monochromator crystal is highly stable. Other X-ray optics applications of diamond channel-cut crystals are anticipated.

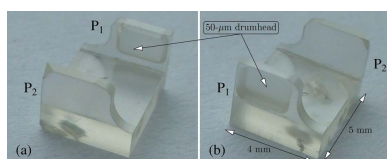
## 1. Introduction

Hard X-ray free-electron lasers (XFELs) in the self-seeding mode (Saldin *et al.*, 2001; Geloni *et al.*, 2011) generate brilliant fully coherent X-ray beams with a well defined and narrow spectrum, typically with a bandwidth of  $\sim 0.2$ – $1$  eV (Amann *et al.*, 2012; Min *et al.*, 2019; Inoue *et al.*, 2019; Nam *et al.*, 2021) and a pulse duration of a few tens of femtoseconds.

When operated in a high-repetition-rate (of the order of megahertz) pulse sequence mode with properly tapered undulators, self-seeded XFELs may deliver X-rays with a pulse energy of  $\sim 10$  mJ per pulse ( $\sim 7 \times 10^{12}$  photons per pulse of  $\sim 10$  keV photons) and a time-averaged power of more than 100 W, corresponding to a time-averaged spectral flux of  $\sim 10^{17}$  photons  $\text{s}^{-1}$  in a bandwidth of  $\sim 1$  eV (Chubar *et al.*, 2016). This flux is about three orders of magnitude larger than the average spectral flux currently possible with storage-ring-based synchrotron radiation sources [see also Yang & Shvyd'ko (2013) and Geloni *et al.* (2015)].

An X-ray source with an increase of three orders of magnitude in the spectral flux opens up exciting new opportunities for hard X-ray spectroscopic techniques, such as inelastic X-ray scattering (Baron, 2016), X-ray photon correlation spectroscopy (Shpyrko, 2014) and nuclear resonant scattering (Rüffer & Chumakov, 2016) in particular.

Such opportunities can be realized today, because high-repetition-rate hard XFELs are now a reality. The European



OPEN ACCESS

XFEL in Hamburg (Germany) (Decking *et al.*, 2020) is the first operational high-repetition-rate XFEL facility. The LCLS-II-HE in Stanford (USA) (Raubenheimer, 2018) is coming soon.

However, these new hard X-ray sources with high average spectral brilliance present not only opportunities but also challenges. One challenge is how to monochromate XFEL beams of very high average and peak power.

To address these challenges, we have designed, manufactured and tested diamond channel-cut crystals for use as high-heat-load beam-multiplexing narrow-band (15 meV bandwidth) mechanically stable monochromators.

A schematic of our channel-cut crystal design, together with relevant X-ray beams, is shown in Fig. 1(a). We choose a channel-cut monolithic monocrystalline design for two reasons. First, this design enables multiple successive Bragg reflections (two, four *etc.*) by perfectly aligned parallel mechanically stable reflecting atomic planes in the reflecting crystal plates  $P_1$  and  $P_2$  of the monolithic system. Second, it ensures parallel propagation of the incident and multiply reflected beams. The design includes a drumhead structure shown in Fig. 1(b) to permit one crystal face to be an ultrathin membrane, as discussed later.

We choose diamond because diamond crystals have a unique combination of outstanding physical properties that are perfect for many X-ray optics applications for which traditional materials, such as silicon, fail to perform (Shvyd'ko *et al.*, 2017). Single crystals of silicon are attractive because they have an almost perfect crystal structure, are commercially available in large quantities and are commonly used in X-ray crystal optics. However, many applications, including those considered here, require better performance than silicon can deliver, specifically, better transparency to X-rays, resilience to radiation damage, mechanical stiffness, X-ray Bragg reflectivity and thermal conductivity. Diamond is the material of choice in such cases, as it is superior to silicon because of its unrivaled radiation hardness, an order of magnitude higher transparency to X-rays, an order of magnitude higher stiffness (Field, 1992; Prelas *et al.*, 1998), orders of magnitude higher thermal conductivity (Wei *et al.*, 1993; Inyushkin *et al.*, 2018), small thermal expansion (Stoupin & Shvyd'ko, 2010, 2011)

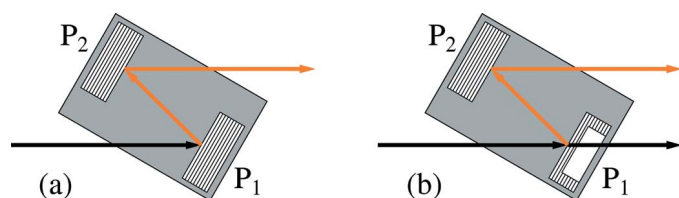


**Figure 1**

Schematic diagrams of monolithic channel-cut crystals with two reflecting crystal plates  $P_1$  and  $P_2$ . Parallel lines in  $P_1$  and  $P_2$  indicate Bragg-reflecting atomic planes. (a) The standard two-plate channel-cut configuration. (b) The design discussed here, featuring a thin crystal membrane in a drumhead structure on plate  $P_1$ . The membrane thickness is sufficient for high Bragg reflectivity in a narrow Bragg-reflection bandwidth and high transmissivity of the out-of-band X-rays.

and almost 100% reflectivity in Bragg diffraction even in backscattering (Shvyd'ko *et al.*, 2010, 2011). This unique combination of outstanding properties makes diamond the most promising material for the transparent resilient high-resolution wavefront-preserving X-ray optics components that are essential for many applications at third-generation light sources. These characteristics are especially important at next-generation high-brilliance high-coherence light sources, such as diffraction-limited storage rings (DLSRs) and XFELs.

The paper is organized as follows. Section 2 covers the function and optical design of the diamond channel-cut crystals. Details of the fabrication are presented in Section 3. The results of characterization of the crystals by X-ray rocking curve imaging are presented in Section 4.1, and the results of X-ray performance tests are given in Section 4.2. Conclusions and outlook are discussed in Section 5.

## 2. Function and optical design

High-repetition-rate (HRR) hard X-ray self-seeded (HXRSS) XFELs will provide X-ray photon beams with an unprecedented spectral flux density advantageous for many applications, in particular for high-resolution spectroscopies, such as nuclear resonant scattering (NRS), inelastic X-ray scattering (IXS) and others. However, dealing with an X-ray beam of such high power is a challenge. Diamond channel-cut crystals can help solve this problem. Our recipe for the solution has four ingredients: a high-indexed Bragg reflection (for a narrow band reflection), diamond crystals (for X-ray transparency and excellent thermomechanical properties), a drumhead design (for low absorbed power and beam sharing) and a monolithic channel-cut design (for in-line geometry and stability).

An important attribute of high-resolution spectroscopies is the use of X-ray beams with millielectronvolt or even sub-millielectronvolt bandwidths. As a result, such techniques require X-ray sources with a high spectral density, and ultra-high-resolution X-ray crystal monochromators with a bandpass of 1–0.1 meV and submicroradian angular stability; see Shvyd'ko (2004) for a review. Such optics usually cannot perform under high-heat-load conditions because of the resulting substantial angular instabilities. At storage-ring synchrotron radiation facilities, additional primary or high-heat-load crystal monochromators are used (Chumakov *et al.*, 2014). This approach reduces the bandwidth of the undulator X-rays to about 1–2 eV and thus reduces substantially (by a factor of  $\sim 100$ ) the heat load on the ultra-high-resolution X-ray crystal monochromators.

However, the standard high-heat-load monochromators are not helpful to deal with X-ray beams generated by HRR–HXRSS XFELs, as these sources typically already have a relatively narrow bandwidth of  $\sim 1$  eV. Rather, such beams require a high-resolution monochromator with a bandpass of  $\sim 10$  meV that is stable under high heat loads. This smaller bandpass would reduce the heat load on the ultra-high-resolution optic by a factor of about 100. As an example,

10 keV X-rays can be monochromated to  $\Delta E \simeq 10$  meV with a single Bragg reflection<sup>1</sup>. In this case, about 1% of the XFEL radiation power in the small bandwidth can be directed to the ultra-high-resolution monochromator and associated spectroscopic experiments. Most of the remaining incident flux is transmitted, rather than being deposited in the crystal, thus avoiding crystal heating, the resulting angular instabilities and, therefore, angular instabilities in the reflected beam. If the monochromator is suitably designed, this remaining flux can be directed to other experiments.

Multiplexing beams from one X-ray source to perform simultaneous experiments is a common approach at synchrotron radiation (Als-Nielsen *et al.*, 1994; Mattenet *et al.*, 1998) and free-electron laser facilities (Zhu *et al.*, 2014; Stoupin *et al.*, 2014; Feng *et al.*, 2015). This multiplexing of the beam requires an X-ray-transparent Bragg-reflecting crystal. Such a crystal would allow most of the incident X-rays, with the exception of the Bragg reflections in the narrow bandwidth, to pass through without absorption. Silicon cannot perform in this way because the ten extinction lengths required for maximum Bragg reflectivity are comparable to the photo-absorption length in silicon. In contrast, for diamond crystals, ten extinction lengths equal about one tenth of the photo-absorption length. Exactly because the extinction length in diamond is much smaller than the absorption length, diamond crystals experience close to 100% Bragg reflectivity, even in backscattering, and simultaneously offer high X-ray transparency (Shvyd'ko *et al.*, 2011). Therefore, we chose to fabricate a diamond crystal membrane with a thickness of about five extinction lengths for high X-ray reflectivity and transparency.

However, this dimension of five extinction lengths measures only about 20 to 100  $\mu\text{m}$ , depending on the chosen Bragg reflection. It is challenging to fabricate and handle such ultrathin crystal components without introducing crystal damage and strain. A solution is to use a drumhead crystal: a monolithic crystal structure comprised of a thin membrane furnished with a surrounding solid collar, shown schematically in Fig. 1(b). This design ensures mechanically stable strain-free mounting of the membrane while still allowing efficient thermal transport (Kolodziej *et al.*, 2016).

Finally, to ensure a fixed direction of the reflected X-rays independent of the Bragg angle, we add one more equivalent Bragg reflection from another crystal plate in a non-dispersive setting, as shown in Fig. 1. To ensure mechanical stability, both crystal plates are a part of a single monolithic channel-cut crystal structure. Channel-cut crystals have been popular in X-ray optics applications since the 1960s (Bonse & Hart, 1965*a,b*, 1966; Deslattes, 1968). Typically they are fabricated from silicon or germanium crystals. Manufacturing a channel-

cut crystal from diamond is a challenge, but becomes possible using modern advanced techniques, as discussed in Section 3.

In the present discussion, we focus on a diamond monolithic channel-cut crystal for use with 14.4125 keV X-rays for <sup>57</sup>Fe nuclear resonant experiments (Gerdau & de Waard, 1999, 2000; Röhlberger, 2004; Ruffer & Chumakov, 2016). We also explored a similar design for use with 12.4 keV X-rays for <sup>45</sup>Sc experiments (Shvyd'ko & Smirnov, 1990).

The 733 Bragg reflection in diamond is the highest indexed reflection that is accessible with 14.4 keV X-rays; it has the largest Bragg angle ( $\theta = 80.75226^\circ$ ) and the smallest Bragg reflection bandwidth (13 meV). However, because of practical considerations related to channel-cut manufacturing (discussed in Section 3), we opted for the reflection with the next highest index, the 800 Bragg reflection, with a smaller Bragg angle of  $\theta = 74.7207^\circ$  and a larger bandwidth of 20 meV.

Fig. 2 shows the predicted X-ray photon energy dependencies of the double 800 Bragg reflection profiles from a diamond channel-cut crystal, calculated numerically using equations of the dynamical theory of X-ray diffraction in crystals (Authier, 2001; Shvyd'ko, 2004). The first and second reflections are from 50 and 500  $\mu\text{m}$ -thick crystal plates, respectively. The peak Bragg reflectivity of the 50  $\mu\text{m}$ -thick crystal reduces to 91%, from 99% for the 500  $\mu\text{m}$ -thick crystal (assuming  $\sigma$  polarization), resulting in a double-reflection peak reflectivity of 89%. The energy bandwidth  $\Delta E$  is 17 meV for the  $\sigma$ -polarization and 14.5 meV for the  $\pi$ -polarization components of the beam. An angular divergence of the incident X-rays of 2.5  $\mu\text{rad}$  (FWHM) is used in the calculations. The calculations show that only 2% of the incident X-ray beam is absorbed in the first plate (the 50  $\mu\text{m}$ -thick diamond drumhead crystal), thus making possible high stability of the monochromator crystal.

Such a diamond monolithic channel-cut crystal can function as a two-bounce 800 Bragg reflection monochromator,

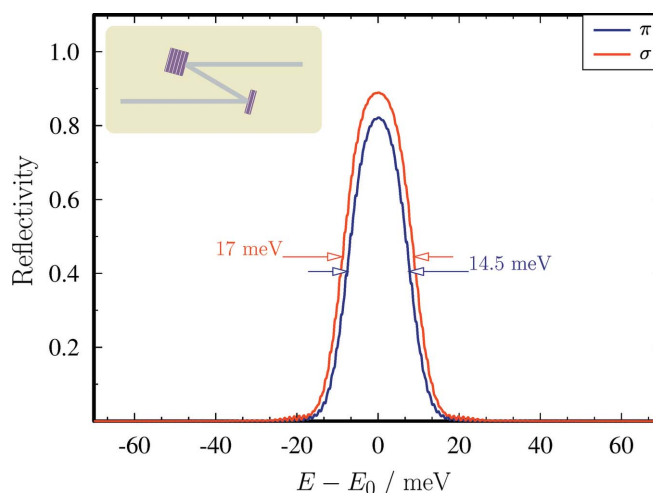


**Figure 2** Diamond crystal reflectivity for X-rays in two successive 800 Bragg reflections calculated as a function of photon energy  $E$  with a central energy,  $E_0 = 14.4125$  keV, corresponding to the nuclear resonance of <sup>57</sup>Fe. The Bragg angle is  $\theta = 74.7207^\circ$ . The photon energy dependences are calculated for two possible X-ray polarization states,  $\pi$  and  $\sigma$ .

<sup>1</sup> XFEL beams typically have a small angular divergence of  $\Delta\theta \simeq 2$   $\mu\text{rad}$  (Saldin *et al.*, 2000; Huang & Kim, 2007). Because of this property, monochromation of X-rays to a  $\sim 10$  meV bandwidth can be achieved with a single high-indexed Bragg reflection, because the spectral broadening due to the angular divergence can be kept small ( $\delta E/E \simeq \Delta\theta/\tan\theta \lesssim 10^{-6}$ ), provided the Bragg angle  $\theta$  is large and  $\tan\theta \gg 1$ . The use of high-indexed Bragg reflections with  $\theta$  close to  $90^\circ$  is therefore important.

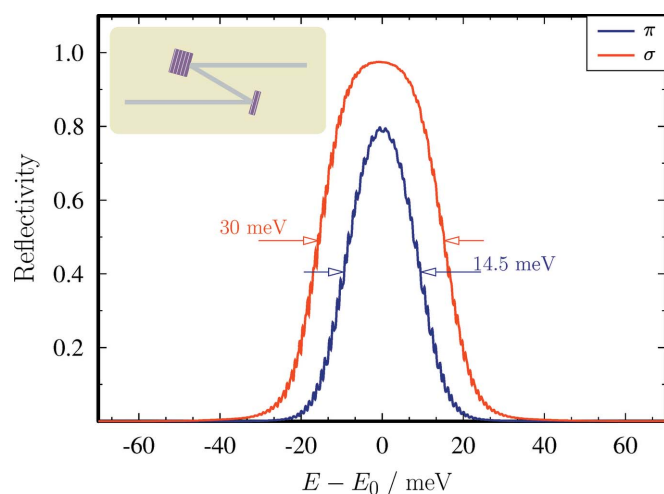


**Figure 3** Diamond crystal reflectivity for X-rays in two successive 620 Bragg reflections calculated as a function of photon energy  $E$  with a central energy,  $E_0 = 12.4$  keV, corresponding to the nuclear resonance in  $^{45}\text{Sc}$ . The Bragg angle is  $62.424^\circ$ .

deflecting 14.4 keV X-rays within a  $\sim 15$  meV bandwidth to  $^{57}\text{Fe}$  nuclear resonant scattering experiments, while the out-band X-rays are transmitted through the thin drumhead crystal and could be transported to a simultaneous experiment<sup>2</sup>.

Similarly, 620 Bragg reflections are suitable for a diamond channel-cut crystal narrow-band monochromator for 12.4 keV X-rays, corresponding to the nuclear resonance in  $^{45}\text{Sc}$  (Shvyd'ko & Smirnov, 1990); see Fig. 3.

### 3. Manufacturing

Two conditions are key to successful realization of a properly functioning diamond channel-cut crystal X-ray monochromator: (i) the availability of flawless single-crystal diamond material in sufficiently large workable sizes, and (ii) the ability to machine diamond without introducing crystal defects.

The characteristic linear dimensions of presently available high-quality synthetic diamond crystals are in the range of a few millimetres [see Shvyd'ko *et al.* (2017) for a recent review]. The crystals are relatively small but sufficient for use with XFEL beams, which are typically less than  $1\text{ mm}^2$  in cross section. Fig. 4 shows a schematic diagram of the diamond channel-cut crystals produced in the present studies.

The channel-cut crystals were cut from synthetically grown raw diamond stones of type IIa (with nitrogen content below 1 p.p.m.). The diamond stones were grown using a temperature-gradient method under high-pressure and high-temperature (HPHT) conditions. The stones used in these

<sup>2</sup>To ensure further stability of such a multiplexed setup, it would be advantageous to choose the scattering plane for the diamond channel-cut crystal to be perpendicular to the scattering plane of the downstream ultra-high-resolution optic, as discussed by Chubar *et al.* (2016).

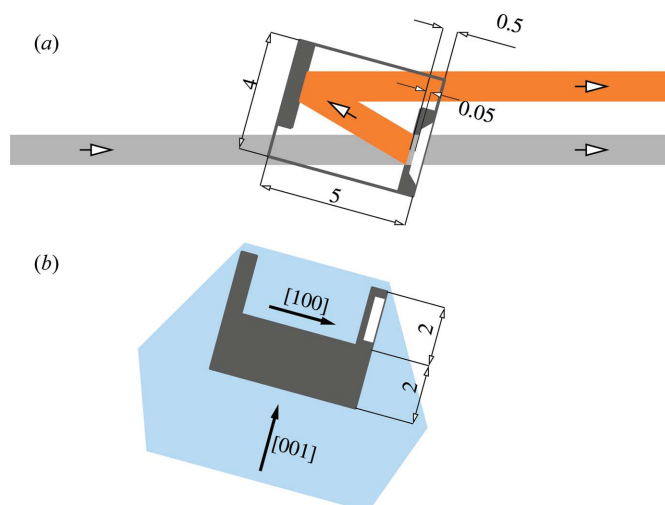


**Figure 4** Schematic diagrams of the (800) diamond channel-cut crystal monochromator for 14.4 keV X-rays (black). The channel cut is machined from an as-grown cubo-octahedral diamond crystal stone (light blue). Shown are (a) top and (b) side views with dimensions in millimetres. The propagation paths of the X-ray beams with a  $1\text{ mm}^2$  cross section are shown in panel (a).

studies were grown and machined at the Technological Institute for Superhard and Novel Carbon Materials (TISNCM) in Troitsk, Russia (Blank *et al.*, 2007; Polyakov *et al.*, 2011).

Raw HPHT-grown diamond stones typically have a cubo-octahedral form. It is well known that the top part of the (001) cubic growth sector (the area furthest from the 001 crystal seed) features the highest crystal quality with the lowest defect density (Burns *et al.*, 2009; Sumiya & Tamasaku, 2012). Therefore, in these studies, the channel-cut crystals are extracted from the top part of the stone, as indicated in Fig. 4(b). With this cut, the crystal plate surfaces parallel to the atomic planes ( $hk0$ ) and to the  $[001]$  direction take the largest volume of highest quality. For this reason, we chose to make an (800) monochromator for use with 14.4 keV X-rays, instead of the narrower band (733) design. Additional reasons for the (800) choice are related to laser machining, as discussed later. Similarly, we chose to make a (620) channel-cut monochromator for 12.4 keV X-rays in the  $^{45}\text{Sc}$  case.

Production of the monochromator crystals begins with selection by visual screening of high-quality as-grown diamond crystal stones for machining. To ensure the fewest defects, crystals with well developed defect-free cubic facets are selected because, as noted previously, the (100) cubic growth sector contains the smallest amount of contamination and lowest number of structural defects. The diamond stones are machined with the newest laser machining technologies.

The monochromator atomic planes [(800) or (620)] of the selected diamond stones are oriented to an accuracy of better than  $0.5^\circ$ , and the channel-cut crystals are cut to the designed shape using a pulsed Nd:YAG laser with the following parameters: 532 nm wavelength (second harmonic), 15 W average power, 10 kHz repetition rate,  $\sim 1.5$  mJ pulse energy, 40 ns pulse duration and  $15\text{ }\mu\text{m}$  focused spot size (FWHM). The

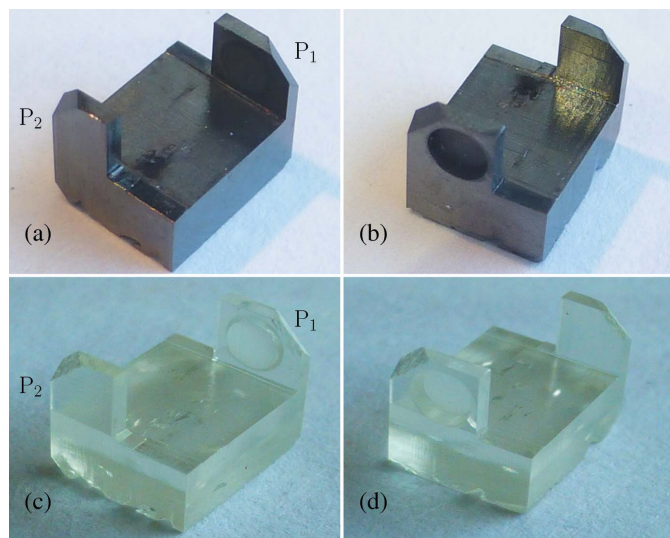


**Figure 5**  
Photographs of the first (800) channel-cut crystal, (a)–(b) taken after laser machining and (c)–(d) taken after annealing in air at 630°C for 3 h.

laser beam is positioned and steered on the workpiece with a two-coordinate optical mirror scanning system equipped with an F-Theta scanning lens. The laser beam is moved with a linear speed of 100 mm s<sup>-1</sup>.

The drumhead structure is formed by layer-by-layer ablation with picosecond pulses from a Nd:YAG laser operated in the third harmonic (355 nm wavelength) with the following parameters: 1 W average power, 10 ps pulse duration, 500 kHz repetition rate and 2 μJ pulse energy. The use of the third harmonic enables reduction of the focused beam spot size and, most importantly, reduction of the diameter of the crater in the diamond produced by a single laser pulse. The crater diameter is 8 μm, provided the beam is focused on the diamond surface. During ablation, the beam is steered over the workpiece at a speed of 150 mm s<sup>-1</sup> with a similar two-coordinate scanning system with an F-Theta lens. The removal rate is about 0.3 μm per layer. The surface roughness of the drumhead surface after laser ablation of a 0.5 mm-thick crystal is ≈ 1 μm (r.m.s.). Similar laser parameters and procedures have been used previously to manufacture diamond X-ray lenses (Terentyev *et al.*, 2015) and drumhead crystals (Kolodziej *et al.*, 2016).

Fig. 5(a) shows photographs of the first machined (800) channel-cut crystal. The crystals appear black after machining. Apparently, laser machining is accompanied by graphitization of the diamond surface. To erase the blackening, we anneal the crystals in air at a temperature of 630–650°C for 3 h, as in our previous and recent studies (Kolodziej *et al.*, 2016; Pradhan *et al.*, 2020). After annealing, the blackening has vanished, as seen on the photographs in Figs. 5(c)–5(d). Most importantly, annealing erases any crystal strain induced in the process of laser cutting or ablation, which is critical for the proper functioning of the channel-cut crystal as a narrow-band X-ray monochromator. The annealing temperature is

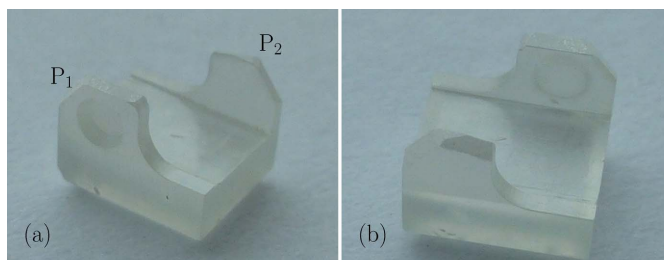


**Figure 6**  
Photographs of the (620) channel-cut crystal after annealing.

chosen such that all residuals of graphite and other carbon compounds are burned in air, while keeping diamond intact (but note that increasing the annealing temperature or time may result in etching of the crystal surface). We will refer to this procedure as medium-temperature in-air annealing (MTA).

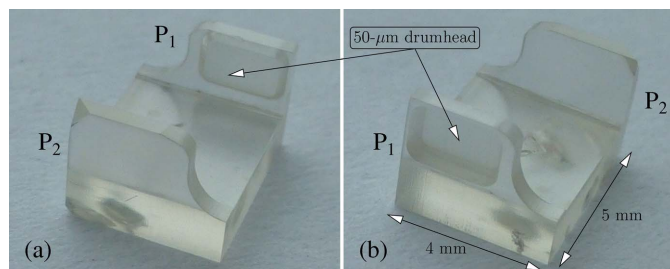
The first reflecting crystal plate of the channel-cut crystal (P<sub>1</sub> in Fig. 5) features a 50 μm-thick drumhead, designed to achieve high reflectivity (≈ 90%) of X-rays in the Bragg reflection band and 98% transmissivity of the out-of-band X-rays. X-rays in the 15 meV band reflected from both crystal plates (P<sub>1</sub> and P<sub>2</sub>) of the channel-cut crystal (see Fig. 2) are directed to a high-spectral-resolution X-ray instrument. The major part, 98% of the incident X-rays in a 1 eV bandwidth (Chubar *et al.*, 2016; Geloni *et al.*, 2015), is transmitted and can be used in simultaneous parallel experiments. The 2 mm-thick base allows the crystal to be mounted mechanically tight and strain-free and to be water-cooled efficiently, ensuring stable operation in high-power XFEL beams.

Fig. 6 shows an example of a (620) diamond channel-cut crystal designed and manufactured for <sup>45</sup>Sc nuclear resonant experiments with 12.4 keV X-rays. The (620) channel-cut crystal also features a 50 μm drumhead on the first plate P<sub>1</sub>. Making drumhead crystals in orientations different from (100) is a challenge (Kolodziej *et al.*, 2016).

Anisotropy of the physical properties of diamond crystals leads to different results in laser ablation of surfaces with different crystal orientations. Surfaces with the (100) orientation do not present significant problems for laser ablation. In contrast, surfaces with the (111) crystallographic orientation are most difficult, both for laser ablation and for polishing. Laser ablation of the (111) surface creates microcracks.

The quality of the (620) surfaces after laser ablation is typically worse than that of the (100) surfaces. We found that increasing the crystal temperature improves the surface quality of the machined surfaces. During machining of the drumhead with the (620) surface orientation, the crystal is heated to 600°C by a resistive heater installed in the crystal holder.

Altogether, three (800) and two (620) channel-cut monochromator crystals were manufactured and characterized. In the following section, we present X-ray characterization results of the best (800) channel-cut crystal monochromator (third iteration), shown in Fig. 7.



**Figure 7**  
Photographs of the best-quality (800) channel-cut monochromator crystal (third iteration) after annealing. Note the optimized rectangular shape of the drumhead  $\sim 2$  mm  $\times$  1.4 mm in size and  $50 \pm 5$   $\mu$ m thick.

## 4. Characterization of channel-cut crystals

### 4.1. Crystal quality test: X-ray rocking-curve imaging

The quality of the diamond channel-cut crystals was characterized using X-ray Bragg diffraction rocking curve imaging (RCI), also known as sequential topography (Lübbert *et al.*, 2000). In this technique, Bragg reflection images of the crystal under study are measured with a pixel X-ray detector, with images being taken sequentially at different incidence angles to the reflecting atomic planes of the well collimated X-rays; Bragg reflection maps are calculated for the reflection peak intensities, angular widths and angular positions. We used an RCI setup (Stoupin *et al.*, 2016; Pradhan *et al.*, 2020) on the X-ray optics testing beamline 1BM (Macrander *et al.*, 2016) at the Advanced Photon Source (APS), shown schematically in Fig. 8.

The RCI setup employs a nearly non-dispersive double-crystal  $C_1$ – $C_2$  arrangement. The first conditioning crystal  $C_1$  is an asymmetrically cut high-quality silicon crystal in the 531 Bragg reflection; the second crystal  $C_2$  is the structure under study, the (800) diamond channel-cut crystal, in the 400 Bragg reflection. We used the 400 Bragg reflection rather than the 800 reflection to characterize the (800) channel-cut crystal for the following reason. We want both reflecting plates  $P_1$  and  $P_2$  of the channel-cut crystal to be illuminated and imaged simultaneously so that we can evaluate whether there is any angular misorientation of the plates due to crystal defects. To meet this requirement, the Bragg angle must be chosen close to  $45^\circ$ , which in turn would require high-energy (19.66 keV)

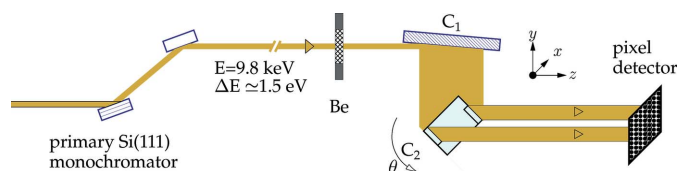


**Figure 8**  
The layout and optical components of the rocking curve imaging setup on the APS bending magnet beamline 1BM, comprising a primary double-crystal Si(111) monochromator, beryllium (Be) window, Si conditioning crystal  $C_1$  in the asymmetric 531 reflection, the diamond (800) channel-cut crystal under study  $C_2$  in the 400 Bragg reflection and the pixel detector. X-rays with a 9.8 keV photon energy and a 1.5 eV bandwidth are used.

X-ray photons if the 800 reflection were used. Such a choice would result in time-consuming measurements, as the photon flux is relatively low at this high photon energy and the angular reflection width ( $\Delta\theta_{800} = 1.2$   $\mu$ rad) is very narrow (compared with  $\Delta\theta_{800} = 5.2$   $\mu$ rad for 14.4 keV X-rays). Therefore, we chose instead the 400 Bragg reflection and 9.831 keV X-rays, for which the Bragg angle  $\theta_{400} = 45^\circ$ , with angular width  $\Delta\theta_{400} = 9.1$   $\mu$ rad if the crystal is 0.5 mm thick (reflecting plate  $P_1$ ) and  $\Delta\theta_{400} = 9.8$   $\mu$ rad if the crystal is 0.05 mm thick (drumhead on reflecting plate  $P_2$ ).

The upstream double-crystal Si(111) monochromator is therefore tuned to select 9.831 keV X-rays. The monochromator bandwidth is  $\sim 1.5$  eV. For the conditioning crystal  $C_1$ , the Bragg angle is  $\theta_{531} = 43.385^\circ$ . The asymmetry angle is chosen as  $\eta_{531} = 41.4^\circ$ , resulting in the asymmetry parameter  $b = -28.7$ . This choice ensures  $\sim 1$   $\mu$ rad angular collimation and an X-ray beam size greater than 20 mm illuminating the channel-cut crystal  $C_2$ . Under these conditions, both plates of the channel-cut crystal are illuminated and can be imaged simultaneously in Bragg diffraction. The setup enables RCI mapping with submicroradian angular and 2.5  $\mu$ m spatial resolution.

X-ray images of the (800) channel-cut crystal taken at the maximum of the sample-integrated Bragg reflection curves are shown in Figs. 9(a) and 10(a). In Fig. 9, X-rays illuminate the front (working) face of plate  $P_1$  and the rear face of plate  $P_2$ , respectively, as in Fig. 7(a). In Fig. 10, the sample is exposed to X-rays from the reverse side, as in Fig. 7(b).

The angular dependencies of Bragg reflectivity (rocking curves) measured with each detector pixel are used to calculate Bragg reflection maps. Figs. 9(b) and 10(b) show color maps of the angular widths (FWHM) of the rocking curves. The color maps of the rocking curves' mid-points are shown in Figs. 9(c) and 10(c). The maps are calculated using a dedicated program (Stoupin, 2015). Cross sections through the FWHM and mid-point maps along the blue lines in Figs. 9(a) and 10(a) are presented in Figs. 9(b'), 9(c'), 10(b') and 10(c'), respectively.

The microscopic defects can be derived from the Bragg reflection FWHM maps. The mesoscopic and macroscopic crystal strain and Bragg plane slope errors can best be evaluated from the mid-point maps. In particular, if the plates of the channel-cut crystal are misoriented due to crystal defects, the mid-point maps will provide this information, because both plates of the channel-cut crystal are imaged simultaneously.

The X-ray images and RCI maps in Figs. 9 and 10 reveal the good crystal quality of the manufactured (800) channel-cut crystal, especially in its upper part. Nevertheless, some defects can be detected. Dislocations and stacking faults are typical defects in HPHT-grown diamond. These defects result in increased angular widths and varying angular positions of the rocking curves. In the center of the plates (in the working area), the angular reflection widths are increased by a few microradians from the expected 9  $\mu$ rad angular width of the 400 Bragg reflection. The angular position of the rocking curves also varies within a range of a few microradians, which

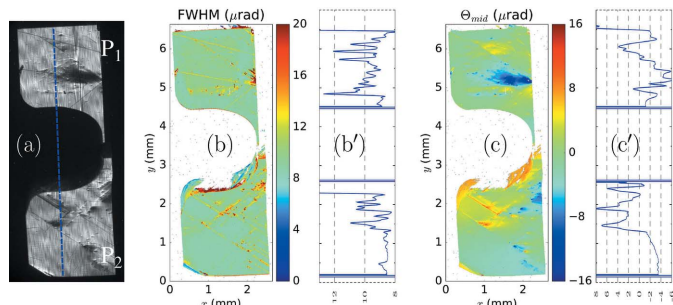


**Figure 9**  
The 400 Bragg reflection X-ray topography and the RCI maps of the diamond (800) channel-cut crystal measured after a second MTA. X-rays illuminate the front face of plate P<sub>1</sub> (drumhead) and the rear face of plate P<sub>2</sub>, respectively, corresponding to Fig. 7(a). (a) X-ray topography taken at the peak of the crystal-integrated rocking curve. (b) and (c) Color maps of the Bragg reflection angular widths (FWHM) and mid-point of the Bragg reflection angular curves (rocking curves), respectively. White pixels indicate that the appropriate values of the FWHM and mid-point are out of the color scale ranges. (b') and (c') Cross-section profiles of color maps (b) and (c), respectively, measured along the blue line indicated in (a). y scales are the same as for (b) and (c), respectively.

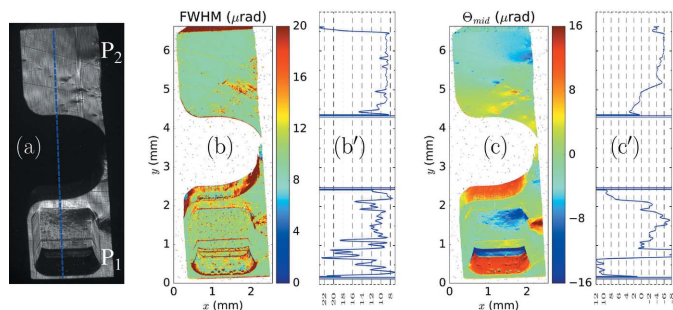


**Figure 10**  
Similar to Fig. 9, but with the channel-cut crystal exposed to X-rays from the reverse side, corresponding to Fig. 7(b).

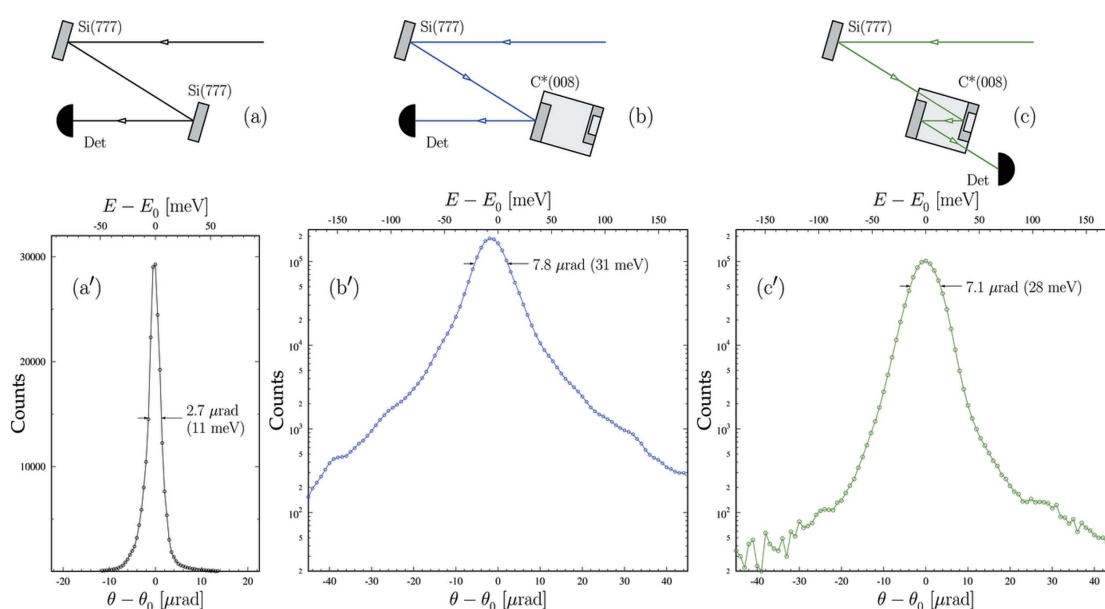


**Figure 11**  
(a), (b) and (c) Schematic diagrams of multi-crystal Bragg diffraction arrangements in non-dispersive settings to measure the angular dependencies of Bragg reflection of 14.41 keV X-rays from (a') a Si(777) crystal, (b') from one (800) plate of the diamond channel-cut crystal and (c') from both plates sequentially, respectively. In all cases X-rays are first reflected from a Si crystal in the (777) Bragg reflection in a non-dispersive setting with regard to the successive Bragg reflections.

indicates angular misalignment of the plates. These distortions are caused chiefly by the crystal defects in the as-grown crystal stone. Machining of the diamond has a secondary effect.

#### 4.2. X-ray performance test: two-bounce Bragg reflection from the diamond channel-cut crystal

The performance of the manufactured (800) diamond channel-cut crystal with a 50 μm drumhead on the first plate P<sub>1</sub> was tested by measuring the angular width Δθ of two successive Bragg reflections of X-rays from its crystal plates P<sub>1</sub> and P<sub>2</sub>. The angular width is measured using a non-dispersive double-crystal arrangement, with the first reference crystal chosen to have an angular reflection width much smaller than the angular width of the channel-cut crystal. The spectral width of the channel-cut double reflection can be estimated as ΔE/E = Δθ/tanθ using the differential presentation of Bragg's law and the measured Δθ value.

We used the 777 Bragg reflection of 14.412 keV X-rays from the reference Si crystal with a Bragg angle of θ<sub>777</sub> = 73.7848° and an angular reflection width of Δθ<sub>777</sub> = 1.2 μrad. It matches well with the 800 Bragg reflection from diamond, with a Bragg angle of θ<sub>800</sub> = 74.7206° and an angular width of Δθ<sub>800</sub> = 5.2 μrad.

In the first step, the setup is tested using two successive 777 Bragg reflections from Si crystals, Si(777) × Si(777), as shown schematically in Fig. 11(a). The angular dependence of the Bragg reflection is measured by rocking the angular orientation of the second crystal and thus changing the angle of incidence of the X-rays to the diffracting atomic planes. The angular reflection profile shown in Fig. 11(a') features an angular width of Δθ<sub>a</sub> = 2.7 μrad, which is close to the expected ~2 μrad. The additional broadening is attributed to the large

horizontal spread of X-rays on a bending magnet beamline. The appropriate spectral bandwidth is calculated to be  $\Delta E_a = E\Delta\theta_a/\tan(\theta_{777}) \simeq 11$  meV. The angular width  $\Delta\theta_a$  and the spectral width  $\Delta E_a$  represent the angular and spectral resolution of the setup with the reference Si(777) crystal.

In the next step, we used a similar nearly non-dispersive double-crystal Bragg reflection arrangement, Si(777)  $\times$  C(800), as shown schematically in Fig. 11(b), to measure the angular width of the single 800 Bragg reflection from one crystal plate of the channel-cut crystal. The reflection profile shown in Fig. 11(b') on a logarithmic scale features an angular width of  $\Delta\theta_b = 7.8$   $\mu$ rad, which is about 2.5  $\mu$ rad broader than the expected value. The broadening is attributed to imperfections in the diamond crystal. The appropriate Bragg reflection spectral width calculated from the differential Bragg law is  $\Delta E_b \simeq 31$  meV, which should be compared with a 20 meV single-reflection spectral width.

In the final step, we used two successive Bragg reflections from both plates of the (800) channel-cut crystal, as shown schematically in Fig. 11(c), to measure the combined angular Bragg reflection width of the channel-cut crystal. Compared with the single-reflection profile in Fig. 11(b'), the double-reflection profile of the channel-cut crystal, shown in Fig. 11(c') on a logarithmic scale, features steeper tails in the angular profile and a narrower angular width of  $\Delta\theta_c = 7.1$   $\mu$ rad. The appropriate Bragg reflection spectral width calculated from the differential Bragg law is  $\Delta E_c \simeq 28$  meV, which is broader than the expected 17 meV (see Fig. 2). The double-reflection peak reflectivity drops by a factor of  $\sim 1.8$  compared with the single-reflection reflectivity in Fig. 11(b'). We attribute the decrease in the double-reflection reflectivity to the angular misorientation of the crystal plates.

Despite the deviations from the theoretical predictions, the manufactured diamond channel-cut crystal is performing within expectations. The experimental data demonstrate the feasibility of using channel-cut diamond crystals to monochromate X-ray beams at cutting-edge XFELs.

## 5. Conclusions and outlook

We have demonstrated the feasibility of diamond channel-cut crystals designed to function as high-heat-load beam-multiplexing narrow-band mechanically stable X-ray monochromators for high-power X-ray beams at cutting-edge high-repetition-rate XFEL facilities. Laser machining techniques were used to manufacture complex 3D structures in the channel-cut crystals. The crystals were designed for use as X-ray monochromators for 14.4 keV X-rays, corresponding to the  $^{57}\text{Fe}$  nuclear resonance, and for 12.4 keV X-rays, corresponding to the  $^{45}\text{Sc}$  nuclear resonance.

The channel-cut crystals were characterized by X-ray rocking curve imaging (topography) and by measurement of the angular and energy widths of double Bragg reflections. The studied channel-cut crystals perform close to theoretical expectations. However, the reflection curves are somewhat broadened and the channel-cut reflecting plates are mis-

oriented by a few microradians because of crystal defects, which further reduces the double-reflection crystal reflectivity.

High crystal quality in the initial diamond stone used in fabricating the channel-cut crystal is essential for the proper functioning of this diamond monochromator.

Along with applications as monochromators, other applications of the diamond channel-cut crystals are anticipated. In particular, because diamond crystals feature very high X-ray reflectivity, they can be used as efficient four-bounce or six-bounce channel-cut polarizers and analyzers to achieve a very high degree of X-ray polarization purity (Bernhardt *et al.*, 2016).

## Acknowledgements

Diamond crystal growth, quality checks and laser machining at FSBI TISNCM were performed on a Shared-Equipment User Facility 'Research of Nanostructured, Carbon and Superhard Materials'.

## Funding information

Work at Argonne National Laboratory was supported by the US Department of Energy, Office of Science, Office of Basic Energy Sciences, under contract DE-AC02-06CH11357.

## References

- Als-Nielsen, J., Freund, A., Grübel, G., Linderholm, J., Nielsen, M., del Rio, M. & Sellschop, J. (1994). *Nucl. Instrum. Methods Phys. Res. B*, **94**, 306–318.
- Amann, J., Berg, W., Blank, V., Decker, F.-J., Ding, Y., Emma, P., Feng, Y., Frisch, J., Fritz, D., Hastings, J., Huang, Z., Krzywinski, J., Lindberg, R., Loos, H., Lutman, A., Nuhn, H.-D., Ratner, D., Rzepiela, J., Shu, D., Shvyd'ko, Yu., Spampinati, S., Stoupin, S., Terentiev, S., Trakhtenberg, E., Walz, D., Welch, J., Wu, J., Zholents, A. & Zhu, D. (2012). *Nat. Photon.* **6**, 693–698.
- Authier, A. (2001). *Dynamical Theory of X-ray Diffraction*. Vol. 11 of *IUCr Monographs on Crystallography*. Oxford University Press.
- Baron, A. Q. R. (2016). *Synchrotron Light Sources and Free-Electron Lasers*, pp. 1643–1757. Cham: Springer International Publishing.
- Bernhardt, H., Marx-Glowna, B., Schulze, K., Grabiger, B., Haber, J., Detlefs, C., Loetzsch, R., Kämpfer, T., Röhlberger, R., Förster, E., Stöhlker, T., Uschmann, I. & Paulus, G. G. (2016). *Appl. Phys. Lett.* **109**, 121106.
- Blank, V., Kuznetsov, M., Nosukhin, S., Terentiev, S. & Denisov, V. (2007). *Diamond Relat. Mater.* **16**, 800–804.
- Bonse, U. & Hart, M. (1965a). *Z. Phys.* **188**, 154–164.
- Bonse, U. & Hart, M. (1965b). *Appl. Phys. Lett.* **6**, 155–156.
- Bonse, U. & Hart, M. (1966). *Z. Phys.* **189**, 151–162.
- Burns, R. C., Chumakov, A. I., Connell, S. H., Dube, D., Godfried, H. P., Hansen, J. O., Härtwig, J., Hoszowska, J., Masiello, F., Mkhonza, L., Rebak, M., Rommevaux, A., Setshedi, R. & Van Vaerenbergh, P. (2009). *J. Phys. Condens. Matter.* **21**, 364224.
- Chubar, O., Geloni, G., Kocharyan, V., Madsen, A., Saldin, E., Serkez, S., Shvyd'ko, Y. & Sutter, J. (2016). *J. Synchrotron Rad.* **23**, 410–424.
- Chumakov, A. I., Sergeev, I., Celse, J.-P., Rüffer, R., Lesourd, M., Zhang, L. & Sánchez del Río, M. (2014). *J. Synchrotron Rad.* **21**, 315–324.
- Decking, W. *et al.* (2020). *Nat. Photon.* **14**, 391–397.
- Deslattes, R. D. (1968). *Appl. Phys. Lett.* **12**, 133–135.
- Feng, Y., Alonso-Mori, R., Barends, T. R. M., Blank, V. D., Botha, S., Chollet, M., Damiani, D. S., Doak, R. B., Glowina, J. M., Koglin, J. M., Lemke, H. T., Messerschmidt, M., Nass, K., Nelson, S., Schlichting, I., Shoeman, R. L., Shvyd'ko, Y. V., Sikorski, M., Song,

- S., Stoupin, S., Terentyev, S., Williams, G. J., Zhu, D., Robert, A. & Boutet, S. (2015). *J. Synchrotron Rad.* **22**, 626–633.
- Field, J. E. (1992). Editors. *The Properties of Natural and Synthetic Diamond*. Cambridge, Massachusetts, USA: Academic Press.
- Geloni, G., Kocharyan, V. & Saldin, E. (2011). *J. Mod. Opt.* **58**, 1391–1403.
- Geloni, G., Kocharyan, V. & Saldin, E. (2015). arXiv:1508.04339.
- Gerdau, E. & de Waard, H. (1999). Editors. *Nuclear Resonant Scattering of Synchrotron Radiation. Hyperfine Interactions*, Vol. 123, pp. 1–879. Springer.
- Gerdau, E. & de Waard, H. (2000). Editors. *Nuclear Resonant Scattering of Synchrotron Radiation. Hyperfine Interactions*, Vol. 125, pp. 1–221. Springer.
- Huang, Z. & Kim, K.-J. (2007). *Phys. Rev. ST Accel. Beams*, **10**, 034801.
- Inoue, I., Osaka, T., Hara, T., Tanaka, T., Inagaki, T., Fukui, T., Goto, S., Inubushi, Y., Kimura, H., Kinjo, R., Ohashi, H., Togawa, K., Tono, K., Yamaga, M., Tanaka, H. & Yabashi, T. I. M. (2019). *Nat. Photon.* **13**, 1749–4893.
- Inyushkin, A. V., Taldenkov, A. N., Ralchenko, V. G., Bolshakov, A. P., Koliadin, A. V. & Katruscha, A. N. (2018). *Phys. Rev. B*, **97**, 144305.
- Kolodziej, T., Vodnala, P., Terentyev, S., Blank, V. & Shvyd'ko, Y. (2016). *J. Appl. Cryst.* **49**, 1240–1244.
- Lübbert, D., Baumbach, T., Härtwig, J., Boller, E. & Pernot, E. (2000). *Nucl. Instrum. Methods Phys. Res. B*, **160**, 521–527.
- Macrander, A., Erdmann, M., Kujala, N., Stoupin, S., Marathe, S., Shi, X., Wojcik, M., Nocher, D., Conley, R., Sullivan, J., Goetze, K., Maser, J. & Assoufid, L. (2016). *AIP Conf. Proc.* **1741**, 030030.
- Mattenet, M., Schneider, T. & Grübel, G. (1998). *J. Synchrotron Rad.* **5**, 651–653.
- Min, C.-K., Nam, I., Yang, H., Kim, G., Shim, C. H., Ko, J. H., Cho, M.-H., Heo, H., Oh, B., Suh, Y. J., Kim, M. J., Na, D., Kim, C., Kim, Y., Chun, S. H., Lee, J. H., Kim, J., Kim, S., Eom, I., Kim, S. N., Koo, T.-Y., Rah, S., Shvyd'ko, Y., Shu, D., Kim, K.-J., Terentyev, S., Blank, V. & Kang, H.-S. (2019). *J. Synchrotron Rad.* **26**, 1101–1109.
- Nam, I., Min, C.-K., Oh, B., Kim, G., Na, D., Young Jin Suh, H. Y., Cho, M. H., Kim, C., Kim, M.-J., Shim, C. H., Jun Ho Ko, H. H., Park, J., Kim, J., Park, S., Park, G., Kim, S., Sae Hwan Chun, H. H., Lee, J. H., Kim, K. S., Eom, I., Rah, S., Deming Shu, K.-J. K., Terentyev, S., Blank, V., Shvyd'ko, Yu., Lee, S. J. & Kang, H.-S. (2021). *Nat. Photon.* **15**, 435–441.
- Polyakov, S. N., Denisov, V. N., Kuzmin, N. V., Kuznetsov, M. S., Martyushov, S. Y., Nosukhin, S. A., Terentiev, S. A. & Blank, V. D. (2011). *Diamond Relat. Mater.* **20**, 726–728.
- Pradhan, P., Wojcik, M., Huang, X., Kasman, E., Assoufid, L., Anton, J., Shu, D., Terentyev, S., Blank, V., Kim, K.-J. & Shvyd'ko, Y. (2020). *J. Synchrotron Rad.* **27**, 1553–1563.
- Prelas, M. A., Popovici, G. & Bigelow, L. K. (1998). Editors. *Handbook of Industrial Diamonds and Diamond Films*. New York: Marcel Dekker Inc.
- Raubenheimer, T. (2018). *Proceedings of the 60th ICFA Advanced Beam Dynamics Workshop (FLS'18)*, 5–9 March 2018, Shanghai, China, pp. 6–11. MOPIWA02.
- Röhlsberger, R. (2004). *Nuclear Condensed Matter Physics with Synchrotron Radiation. Basic Principles, Methodology and Applications*. Vol. 208 of *Springer Tracts in Modern Physics*. Berlin-Heidelberg: Springer Verlag.
- Rüffer, R. & Chumakov, A. (2016). *Synchrotron Light Sources and Free-Electron Lasers*, pp. 1–32. Cham: Springer International Publishing.
- Saldin, E. L., Schneidmiller, E. A., Shvyd'ko, Yu. V. & Yurkov, M. V. (2001). *Nucl. Instrum. Methods Phys. Res. A*, **475**, 357–362.
- Saldin, E. L., Schneidmiller, E. A. & Yurkov, M. V. (2000). *The Physics of Free Electron Lasers. Advanced Texts in Physics*. Berlin Heidelberg: Springer.
- Shpyrko, O. G. (2014). *J. Synchrotron Rad.* **21**, 1057–1064.
- Shvyd'ko, Yu. (2004). *X-ray Optics – High-Energy-Resolution Applications*, Vol. 98 of *Optical Sciences*. Berlin: Springer.
- Shvyd'ko, Yu., Blank, V. & Terentyev, S. (2017). *MRS Bull.* **42**, 437–444.
- Shvyd'ko, Yu. V. & Smirnov, G. V. (1990). *Nucl. Instrum. Methods Phys. Res. B*, **51**, 452–457.
- Shvyd'ko, Yu. V., Stoupin, S., Blank, V. & Terentyev, S. (2011). *Nat. Photon.* **5**, 539–542.
- Shvyd'ko, Yu. V., Stoupin, S., Cunsolo, A., Said, A. & Huang, X. (2010). *Nat. Phys.* **6**, 196–199.
- Stoupin, S. (2015). *Python-DTAXRD*, <https://www.aps.anl.gov/Science/Scientific-Software/DTAXRD>.
- Stoupin, S., Shvyd'ko, Yu., Trakhtenberg, E., Liu, Z., Lang, K., Huang, X., Wieczorek, M., Kasman, E., Hammonds, J., Macrander, A. & Assoufid, L. (2016). *AIP Conf. Proc.* **1741**, 050020.
- Stoupin, S. & Shvyd'ko, Yu. V. (2010). *Phys. Rev. Lett.* **104**, 085901.
- Stoupin, S. & Shvyd'ko, Yu. V. (2011). *Phys. Rev. B*, **83**, 104102.
- Stoupin, S., Terentyev, S. A., Blank, V. D., Shvyd'ko, Y. V., Goetze, K., Assoufid, L., Polyakov, S. N., Kuznetsov, M. S., Kornilov, N. V., Katsoudas, J., Alonso-Mori, R., Chollet, M., Feng, Y., Glowonia, J. M., Lemke, H., Robert, A., Sikorski, M., Song, S. & Zhu, D. (2014). *J. Appl. Cryst.* **47**, 1329–1336.
- Sumiya, H. & Tamasaku, K. (2012). *Jpn. J. Appl. Phys.* **51**, 090102.
- Terentyev, S., Blank, V., Polyakov, S., Zholudev, S., Snigirev, A., Polikarpov, M., Kolodziej, T., Qian, J., Zhou, H. & Shvyd'ko, Yu. (2015). *Appl. Phys. Lett.* **107**, 111108.
- Wei, L., Kuo, P. K., Thomas, R. L., Anthony, T. R. & Banholzer, W. F. (1993). *Phys. Rev. Lett.* **70**, 3764–3767.
- Yang, X. & Shvyd'ko, Yu. (2013). *Phys. Rev. ST Accel. Beams*, **16**, 120701.
- Zhu, D., Feng, Y., Stoupin, S., Terentyev, S. A., Lemke, H. T., Fritz, D. M., Chollet, M., Glowonia, J. M., Alonso-Mori, R., Sikorski, M., Song, S., van Driel, T. B., Williams, G. J., Messerschmidt, M., Boutet, S., Blank, V. D., Shvyd'ko, Yu. V. & Robert, A. (2014). *Rev. Sci. Instrum.* **85**, 063106.